Uncertainty assessment of the Ring of Fire concept for on-site aerodynamic drag evaluation

Spoelstra, A.M.C.M.G.; Hirsch, Maximilian; Sciacchitano, A.; Scarano, F.

DOI
10.1088/1361-6501/abb50d

Publication date
2020

Document Version
Final published version

Published in
Measurement Science and Technology

Citation (APA)
Spoelstra, A. M. C. M. G., Hirsch, M., Sciacchitano, A., & Scarano, F. (2020). Uncertainty assessment of the Ring of Fire concept for on-site aerodynamic drag evaluation. *Measurement Science and Technology*, *32*(4), Article 044004. https://doi.org/10.1088/1361-6501/abb50d

Uncertainty assessment of the Ring of Fire concept for on-site aerodynamic drag evaluation

OPEN ACCESS
IOP Publishing
Measurement Science and Technology
Meas. Sci. Technol. **32** (2021) 044004 (14pp)
https://doi.org/10.1088/1361-6501/abb50d

Uncertainty assessment of the Ring of Fire concept for on-site aerodynamic drag evaluation

A Spoelstra, M Hirsch, A Sciacchitano and F Scarano

Delft University of Technology, Aerospace Engineering Department

E-mail: a.m.c.m.g.spoelstra@tudelft.nl

Received 26 May 2020, revised 10 July 2020
Accepted for publication 3 September 2020
Published 15 February 2021

Abstract

The Ring of Fire (RoF) measurement concept to perform on-site experiments of aerodynamic drag for transiting objects is investigated with a study that identifies the main sources of uncertainty.

The main contributors to the uncertainty of the drag measurement are examined for the case of a cyclist riding through the measurement domain. A sensitivity analysis is conducted that assesses how the estimated drag is affected by the choice of particle image velocimetry image processing parameters. The size of the cross-section considered in the control volume formulation is also investigated. It is found that the accuracy of the estimated drag depends on the procedure used to detect the edge of the momentum deficit region in the wake. Moreover imposing mass conservation yields the most accurate drag measurements. The drag estimation has little dependence upon the spatial resolution of the measurement as long as the interrogation window size stays within 5% to 25% of the equivalent diameter of the object cross section. Experiments are conducted in a sport-hall, where the aerodynamic drag estimates from the RoF are compared to a conventional torque power meter installed on the bicycle, and different rider's postures as well as equipment variations are considered. Although the discrepancy in the absolute value of drag can be as high as 20%, power metering and RoF agree within 4% on relative drag variations.

Supplementary material for this article is available online

Keywords: large-scale PIV, helium filled soap bubbles, uncertainty PIV, cycling aerodynamics, on-site aerodynamic measurements

(Some figures may appear in colour only in the online journal)

1. Introduction

Aerodynamic loads measurements and optimisation are relevant in a broad variety of sectors, including aeronautics and ground transportation, animal flight, and speed sports. Several approaches for measuring the aerodynamic forces, particularly drag, have been proposed in the past, including wind tunnel measurements (Jones 1936, Zdravkovich 1990, Laitone 1997), towing force measurements (von Carmer *et al* 2008, Tschepe *et al* 2019), on-site measurements (Le Good *et al* 1998, Matschke and Heine 2002, Edwards and Byrnes 2007, Usherwood *et al* 2020) and numerical simulations by Computational Fluid Dynamics (Griffith *et al* 2014, Khayrullina *et al* 2015). Wind tunnel experiments often feature scaled models where the aerodynamic loads are measured with a force balance (Watkins *et al* 1992). Uncertainties typically arise from scaling effects, relative-to-ground motion modelling,

model blockage and often interference of the support (Barlow *et al* 1999, Páscoa *et al* 2012). Furthermore, some specific cases such as the study of accelerating or decelerating conditions (Coutanceau and Bouard 1977) are difficult to reproduce in the wind tunnel environment. Finally, the development of the wake over a large distance (Scarano *et al* 2002, Bell *et al* 2015) or the study of the biomechanics of flight (Spedding and Hedenström 2010, Hedenström and Johansson 2015) are not easily conducted in wind tunnels. In some of the above cases, conducting measurements with the object moving through a quiescent fluid has been pursued. For instance, Henning *et al* (2016) carried out particle image velocimetry (PIV) measurements in the lateral underfloor region of a full-scale high-speed train transiting at 44 m s^{-1}; in their investigation, the high speed of the train and the corresponding Reynolds number ($Re = 9 \times 10^6$) were crucial for the so-called ballast projection to occur. When the primary interest of the measurements is not the flow visualisation but rather the evaluation of the aerodynamic drag, the steady state torque test and the coast-down technique are established methods of determining on-road aerodynamic drag of for road vehicles (Passmore and Jenkins 1988) and of cyclists (Debraux *et al* 2011).

In recent years, the steady state torque test became the most practiced method in cycling. Power meter measurements are carried out to determine the power output of the cyclist, from which the cyclist's aerodynamic drag is retrieved based on the balance of power (Grappe *et al* 1997). When comparing these on-site techniques with wind tunnel measurements, the advantages of more realistic flow conditions and lower costs are counterbalanced by an increased uncertainty due to additional error sources, such as the less-controlled atmospheric conditions and the physical modelling of non-aerodynamic resistance forces, e.g. due to rolling resistance and drive train losses. Moreover, the on-site techniques adopted so far do provide direct access to the aerodynamic drag, but with no indication of the flow behaviour. The latter is necessary when the physical sources of aerodynamic drag need to be identified and possibly minimised.

In the recent years, a measurement concept has been introduced by the authors' group (Terra *et al* 2017, 2018, Spoelstra *et al* 2019), namely the Ring of Fire (RoF), based on large-scale stereoscopic PIV measurements past an object or a vehicle travelling through a quiescent environment. The analysis of the momentum difference between the conditions prior to and after the transit poses the basis to estimate the aerodynamic drag. This measurement approach has been used to estimate the aerodynamic drag of cyclists during outdoor and indoor sport action returning a quantitative visualization of the flow field in the wake (Spoelstra *et al* 2019).

Knowledge of the drag resolution, or minimum detectable drag variation, is relevant when measurements are intended to perform aerodynamic optimisation. Terra *et al* (2018) studied the drag resolution of a small-scale RoF system analysing the drag of a towed sphere in a narrow range of velocities, under the assumption of constant drag coefficient. Spoelstra *et al* (2019) attempted drag estimates from a large-scale RoF. The comparison with literature data could not yield a conclusive assessment, given the large dispersion (approx. 50%) of the data due to many varying parameters, like rider posture, bikes geometries and testing conditions.

Although a number of RoF experiments have returned wake measurements that agree satisfactorily with wind tunnel data, the uncertainty of the measured drag and its dependency upon experimental conditions and the image processing parameters have not yet been addressed. In particular, the errors arising from the set-up of the PIV measurement, the image recording and analysis, as well as the application of the control volume approach require a detailed scrutiny to support best practice of experiments.

In this work, linear error propagation is applied to determine how the uncertainty of the measured velocity field affects the drag calculation. Furthermore, the effect of the above-mentioned PIV parameters is investigated.

The drag resolution of the RoF is studied here during large-scale indoor experiments by comparison with simultaneous power meter measurements. Absolute and relative drag variations are introduced by different cyclist postures, as well as varying garments.

2. Drag evaluation techniques

This section discusses the principles of drag measurement by use of the integrated power meter and from the Ring of Fire velocity measurements. The example of a cyclist is considered here, although the conclusions can be extended to other problems such as ground vehicles and speed sports in general.

2.1. Power meter

A cyclist travelling on a flat, horizontal road imparts a force $F_{cyclist}$ to sustain the motion contrasted by resistive forces, namely the aerodynamic drag D_{aero}, external ($D_{rolling}$) and internal frictional forces ($D_{friction}$ for the drive-train and $D_{bearing}$ for the wheels). Any unbalance between these forces results in acceleration or deceleration of the cyclist (ma).

$$ma = F_{cyclist} - D_{rolling} - D_{friction} - D_{bearing} - D_{aero} \quad (1)$$

To extract the aerodynamic drag from the total drag value, the other terms are usually modelled by use of semi-empirical expressions. Following the methods described in Martin *et al* (1998) and Lukes *et al* (2012), the aerodynamic drag can be obtained by:

$$D_{aero} = \underbrace{\eta_{drivetrain}}_{\text{Drivetrain efficiency}} \cdot \underbrace{\frac{P_{cyclist}}{u_C}}_{\text{Total resistance}} - \underbrace{ma}_{\text{Inertia}} - \underbrace{C_{rr}\left(m\frac{{u_C}^2}{r_m}\cos\alpha + mg\sin\alpha\right)}_{\text{Rolling resistance}} - \underbrace{(91 + 8.7u_C)\cdot 10^{-3}}_{\text{Wheel bearing resistance}} \quad (2)$$

Where $\eta_{drivetrain}$ is the drivetrain efficiency, $P_{cyclist}$ is the mechanical power generated by the cyclist, u_C is the cyclist velocity in quiescent air, C_{rr} is the rolling friction coefficient,

m is the combined mass of rider and bike, g is the gravitational acceleration, r_m is the radius of curvature for the centre of mass trajectory and α is the cyclist's lateral lean angle relative to the horizon. The term $m\frac{u_C^2}{r_m}\cos\alpha$ accounts for the case where the cyclist moves along a curvilinear path of the radius of curvature r_m. When the cyclist rides along a straight path, the expression of the aerodynamic drag simplifies to:

$$D_{aero} = \underbrace{\eta_{drivetrain}}_{\text{Drivetrain efficiency}} \cdot \underbrace{\frac{P_{cyclist}}{u_C}}_{\text{Total resistance}} - \underbrace{ma}_{\text{Inertia}} - \underbrace{C_{rr}mg}_{\text{Rolling resistance}} - \underbrace{(91+8.7u_C)\cdot 10^{-3}}_{\text{Wheel bearing resistance}} \tag{3}$$

The drivetrain efficiency varies between 96% and 98% for power outputs in the range 50–200 W (Kyle 2001, Spicer *et al* 2001). The rolling resistance coefficient is dependent on the tyre-pressure, -loading, -diameter and -temperature, as well as the surface properties of the ground and the steering conditions (Burke 2003). Grappe *et al* (1997) and Baldissera and Delprete (2016) regard the effect of speed on the rolling coefficient in cycling as negligible and therefore use a speed-invariant C_{rr} value.

2.2. Ring of Fire measurement principle

The drag evaluation through the Ring of Fire has been described in two previous studies from (Terra *et al* 2017, Spoelstra *et al* 2019). Conservation of momentum is invoked for the stationary problem in a control volume around a moving object. The difference of momentum flux results in the drag force D. When the control volume extends sufficiently upstream and downstream of the transiting object, it can be shown that the viscous stresses are negligible (Kurtulus *et al* 2007) and the drag force can be obtained from the surface integral over the inlet and outlet surfaces as illustrated in figure 1 (Rival and Oudheusden 2017). The measurements are conducted in a fixed frame of reference (that of the laboratory) where the cyclist moves at constant speed u_C across the measurement region. As discussed in the initial study of the RoF (Spoelstra *et al* 2019), air prior to the passage of the cyclist features inevitable small chaotic motions due to the disturbances in the environment (atmospheric wind, residual motions from previous passages, as depicted in figure 1). The velocity of such motions is denoted as u_{env}. After the passage of the cyclist, the flow velocity features a coherent wake with a velocity distribution u_{wake} as a result of the air entrainment produced by the cyclist. The variation of momentum written in the cyclist frame of reference, results in the following expression for the instantaneous drag (Terra *et al* 2017):

$$D(t) = \underbrace{\rho \iint_{S_1} (u_{env}-u_C)^2 dS + \iint_{S_1} p_1 dS}_{1} \underbrace{- \rho \iint_{S_2} (u_{wake}-u_C)^2 dS - \iint_{S_2} p_2 dS}_{2} \tag{4}$$

where ρ is the air density. This expression is valid at the condition that the mass flow is conserved across surfaces S_1 and S_2. Time averaging is performed for every single passage with the objective of reducing the effect of the unsteady fluctuations.

$$\overline{D}_{\text{single}} = \frac{1}{M}\sum_{i=1}^{M} D_i(t) \tag{5}$$

Where M is the total number of time instants composing the measurement. It has been shown in previous works that the unsteady behaviour in the wake of bluff objects typically considered for RoF measurements (Terra *et al* 2017, Spoelstra *et al* 2019) prevents the accurate estimate of the aerodynamic drag from one single passage. Therefore, ensemble averaging from multiple passages is required to achieve statistical convergence of the drag estimate.

$$\overline{D}_{\text{multi}} = \frac{1}{N}\sum_{j=1}^{N} \overline{D}_{\text{single},j} \tag{6}$$

where N is the number of passages.

3. Experimental setup and protocol

3.1. Test facility and subject

Experiments were conducted in a spacious indoor facility (figure 2) 39 m wide and 77 m long, with flat concrete surface. The cyclist rode loops of 190 m length in clockwise direction. The lap can be described as two semi-circles with a radius of 17.8 m, connected by two 39 m long straights. The start point of each lap is located at x= 0 m.

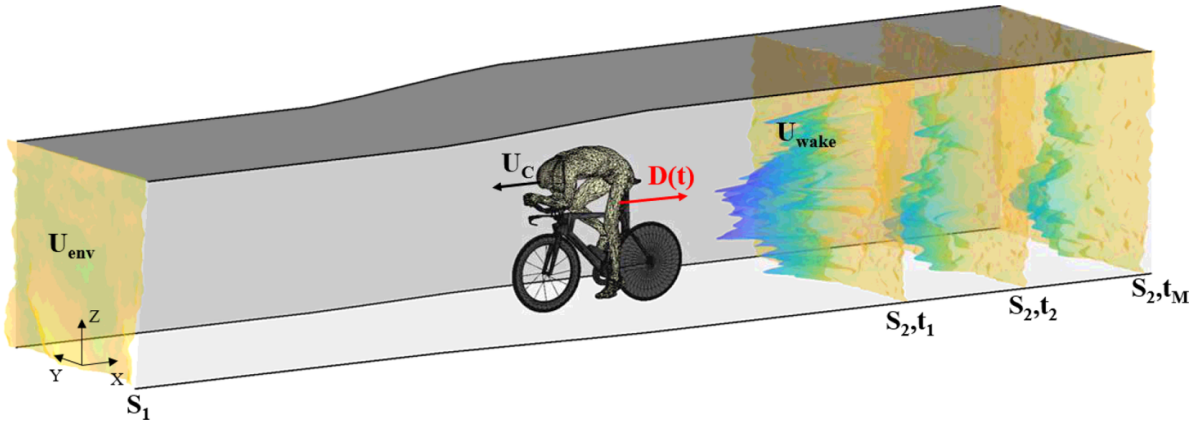

Figure 1. Schematic view of the velocity distribution before and after the passage of the cyclist.

The rider was a professional athlete; his body mass and height were 79 kg and 187 cm, respectively, and his shoulder width was equal to 50 cm. He wore a short leg and short arm time trial skin suit from Team Sunweb. Two helmet types were tested as shown in figure 3. The rider wore over-shoes extending to half of their calves, as well as laser protection goggles.

A Team Sunweb time trial bike, model Trinity Advanced SL 2018 from Giant was used during experiments of 1.7 m length and 8.8 kg weight. The rear wheel was a PRO Tubular disc. The wheels mounted a Tubular Vittoria Corsa G 23 mm tyre set at 5 bar pressure. The estimated rolling resistance coefficient for this tire and conditions is $C_{rr} = 0.0045$ (Bierman 2016). The cyclist's velocity was monitored with a magnetic sensor. A magnet was placed on the rear wheel of the bike and scanned by a magnetic sensor to retrieve information about displacement and velocity. The bike GPS device stored these data with a frequency of 1 Hz.

The cyclist maintained a constant speed of 8.3 m s^{-1}, with a normalised pedalling frequency (Crouch *et al* 2014) of $k = 2\pi rf/u_c = 0.15$, where r is the bike crank length, f the cadence and u_c the cyclist velocity. Three different configurations were examined (see figure 3): (1) the cyclist in upright position with an aerodynamic helmet; (2) the cyclist in time trial position with the same helmet and (3) the cyclist in time trial position with a road helmet. For each configuration, measurements were collected during 40 loops to build an ensemble average estimate of the aerodynamic drag from the RoF and gather data from the power meter installed on the bicycle.

3.2. Power meter measurement system

The bike was equipped with an SRM *Road Pro* crank-spider-based power, widely regarded as the benchmark for power meter devices (Duc *et al* 2007, Passfield *et al* 2017). The device recorded concurrent measurements of the athlete's mechanical power output, ground velocity and cadence in time. Before commencing trials, all units used during testing were calibrated against a zero torque reference, while pedals were stationary and unloaded as indicated by the manufacturer. For the calculation of ground velocity, the measured wheel circumference value of 2096 mm was used. Using an external torque dynamometer, the 95% confidence level uncertainty of the SRM power meter was estimated as 2% of the measured value over a range of 0–4096 W (Bertucci *et al* 2005). After each complete crank revolution, power and cadence measurements were obtained. Data was recorded by the head unit at a rate of 1 Hz after being linearly interpolated in time (Underwood 2012).

3.3. Ring of Fire measurement system

Velocity measurements upstream and downstream of the cyclist were performed with a large-scale stereoscopic-PIV system based on neutrally buoyant helium-filled soap bubbles (HFSB) of 0.3 mm diameter (Bosbach *et al* 2009). The tracers were produced by a 200 nozzles rake installed inside the tunnel. A LaVision HFSB fluid supply unit (FSU) controls soap, air and helium flow rates supplied to the seeding rake. A 10 m long tunnel structure of 4 × 3 m^2 cross-section was built that confines the tracers around the measurement plane. The tunnel was built out of wooden panels integrated in an aluminium frame. Experiments were performed at a tracer concentration of approximately 13 bubbles/cm^3. To quantify the tracing fidelity, the tracer's Stokes number, S_t, is considered, which is defined as the ratio of the tracer response time, τ_p, over the flow characteristic time, τ_f. Samimy and Lele (1991) showed that a particle is a faithful flow tracer when the condition $S_t < 0.1$ is satisfied. Based on previous studies from our group (Scarano *et al* 2015, Faleiros *et al* 2019), the helium-filled soap bubbles feature a tracer response time in the order of 10 to 100 μs, yielding a tracer's Stokes number in the order of 10^{-3} based on cyclist torso length and velocity. The light source was a Quantel Nd:YAG *Evergreen 200* laser (2 × 200 mJ at 15 Hz). A laser sheet thickness of 5 cm was selected to guarantee a sufficient number of tracer particles in each interrogation window, as well as to comply with the one-quarter rule (Raffel *et al* 2018) when images were recorded with $\Delta t = 2$ ms pulse separation. Based on the study of Terra *et al* (2019), a maximum out-of-plane velocity of 5 m s^{-1} was expected in the cyclist's wake, thus requiring a laser sheet thickness of at least 4 cm to comply with the one-quarter rule. It should be noted that the selected laser

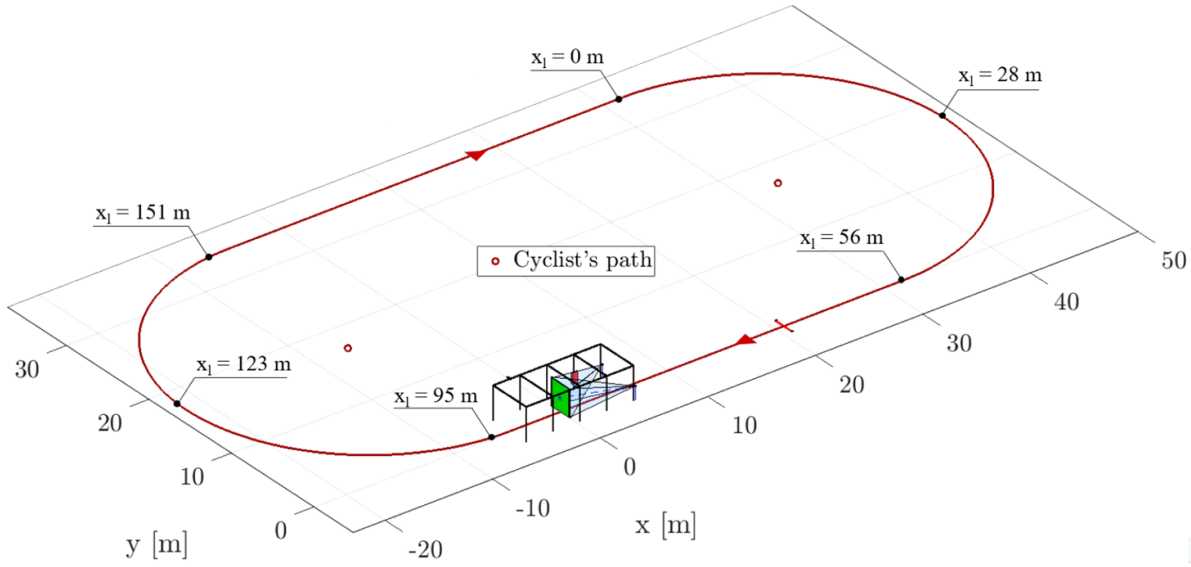

Figure 2. Isometric view of the testing facility and measurement apparatus layout.

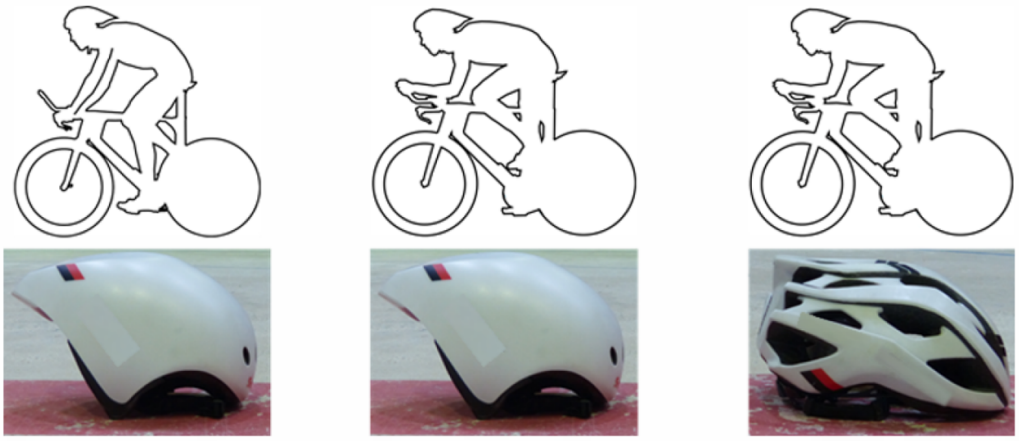

Figure 3. Riding configurations and helmets used. Upright position with aerodynamic helmet (left). Time trial position with aerodynamic helmet (middle). Time trial position with conventional road helmet (right).

sheet thickness is about 1/40th of the in-plane dimensions of the measurement domain, which is consistent with many PIV experiments conducted at smaller scale (Raffel *et al* 2018). Two LaVision *Imager sCMOS* cameras (2560 × 2160 pixels at 50 fps, 16 bit, pixel pitch 6.5 μm) were equipped with AF Nikkor 35 mm objectives and daylight optical filters. A lens-tilt mechanism allowed complying with the Scheimpflug condition for in-focus imaging in stereoscopic conditions. The lens aperture was set to $f_{\#} = 8$ ensuring that particles in the illuminated region were imaged in focus. The cameras were placed 5.2 m upstream of the measurement plane at a relative angle of 35 degrees. The field of view captured by both cameras was 2.4 × 1.9 m^2, yielding a magnification factor $M = 0.0065$ and a digital imaging resolution of 1.01 px mm^{-1}. The measurements were synchronised with the transit of the athlete using a photodetector (PHD) placed 20.5 m upstream of the measurement plane, which triggers the PIV system through a LaVision programmable time unit (PTU 9). Image pairs were acquired at a rate of 15 Hz with a pulse separation time of $\Delta t = 2$ ms. A detailed sketch of the RoF setup is shown in figure 4.

3.4. Measurement protocol

The PIV system and SRM power meter were calibrated at the beginning of each measurement day. Bubbles production was initiated about two minutes before the start of each run to achieve a uniform tracer distribution with sufficient concentration in the measurement domain. The cyclist started riding from the opposite side of the hall with respect to the measurement region, accelerating to the desired speed of 8 m s^{-1}. At each lap the image acquisition was triggered by the PHD, after which 40 image pairs are recorded and saved to a mass storage device before the next lap (typically 20 s). For all tests, all the doors of the hall were closed to minimise externally generated airflows. However, as the cyclist circled the hall, the induced air entrainment resulted in some systematic tailwind. The latter effect is unwanted, first as it tends to transport the seeding

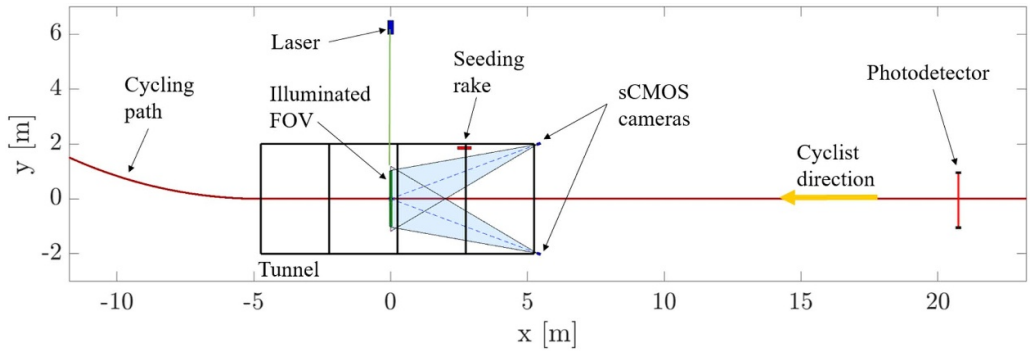

Figure 4. Schematic representation of the experimental layout of the RoF.

particles out of the RoF-tunnel, and secondly because it introduces larger fluctuations in the air motions prior to the passage of the cyclist. This effect was mitigated by carrying a blanket through the tunnel in the opposite direction after every passage. A movie recorded during the experimental campaign is available online.

4. Data processing

4.1. Power meter

The power output and measured bike velocity of all runs are post-processed to obtain instantaneous drag area values. The power meter data are synchronised with the data recorded from the PIV measurements, including the time stamp of the laser illumination at the cyclist passage. Traces of velocity and power around the track are shown in figure 5 for the individual upright measurements. Besides the individual traces of each loop, the mean value of all loops is included.

The mean velocity and mean power during the lap vary by approximately 5% and 45%, respectively. The loop-to-loop variations are up to 10% for the velocity and 70% for the power. Olds (2001) and Lukes *et al* (2012) have discussed the relation between these variations and the movement of the centre of gravity (CG) towards the centre of the track during corners. Due to this movement, the CG travels at lower speed than the tyre contact point. Therefore, the comparison to the RoF is based on the power and velocity data recorded within the straight segment that includes the RoF measurement station (dotted box in figure 5). Within this portion, the relative variation of mean velocity and power stays within 1% and 8% respectively.

An additional correction needed for the power meter needs to account for the velocity of the air (u_{env}). The model as described by equation (3) assumes surrounding air at rest to calculate drag from power and velocity. The relative velocity between cyclist and air is estimated by PIV measurements prior to the cyclist passage.

4.2. Ring of Fire: particle image velocimetry

The recorded images are analysed with the LaVision *DaVis* 8 software. Background light is removed by subtracting an image taken in absence of seeding. Particle intensity is homogenised by a min/max-filter (Westerweel 1993). The two-frame recordings are interrogated with iterative cross-correlation algorithm with window deformation (Scarano 2001). The initial interrogation window (IW) size is at least equal to or larger than ¼ of the particles image displacement (Adrian & Westerweel, 2011), whereas the final interrogation window size is varied to study the effects of spatial resolution (section 5.3). Spurious vectors identification is based on the universal outlier detection method proposed by Westerweel and Scarano (2005). To assess the out-of-plane velocity scales that the PIV system is able to resolve, the dynamic velocity range (DVR, (Adrian 1997)) is determined as the ratio between the maximum velocity in the near wake of the cyclist ($\approx$8 m s^{-1}) and the standard deviation of the velocity distribution in the quiescent flow prior to the cyclist's passage ($\approx$0.03 m s^{-1}). This leads to a DVR of 266.

The results are presented in the coordinate system as shown in figures 1 and 2. Non-dimensional relative velocity and non-dimensional time are defined respectively as:

$$u_x^* = \frac{u_{\text{wake}} - u_{\text{env}} - |u_C|}{|u_C|} \qquad t^* = \frac{t \times |u_C|}{D} \tag{7}$$

where $c = 0.5$ m is the shoulder width of the cyclist and $t = 0$ is the time instant when the rearmost point of the bicycle saddle crosses the laser sheet

4.3. Ring of Fire: control volume approach

4.3.1. Wake identification. The evaluation of the cyclist drag via the control volume approach requires the flow velocity measurements before and after the passage of the cyclist. In the ideal case when the cyclist is moving through quiescent air and the velocity measurements are noise-free, the drag estimate is not affected by the cross-sectional size of the control volume. However, in practice, environmental flow fluctuations and noise in the velocity measurements affect the estimated drag value and, based on equation (4) and as discussed in more detail in section 5.1, their effect increases with increasing size of the cross-sectional areas S_1 and S_2. Hence, a dedicated wake contouring approach is applied, which isolates the cyclist's wake from the outer flow region. Several steps are performed

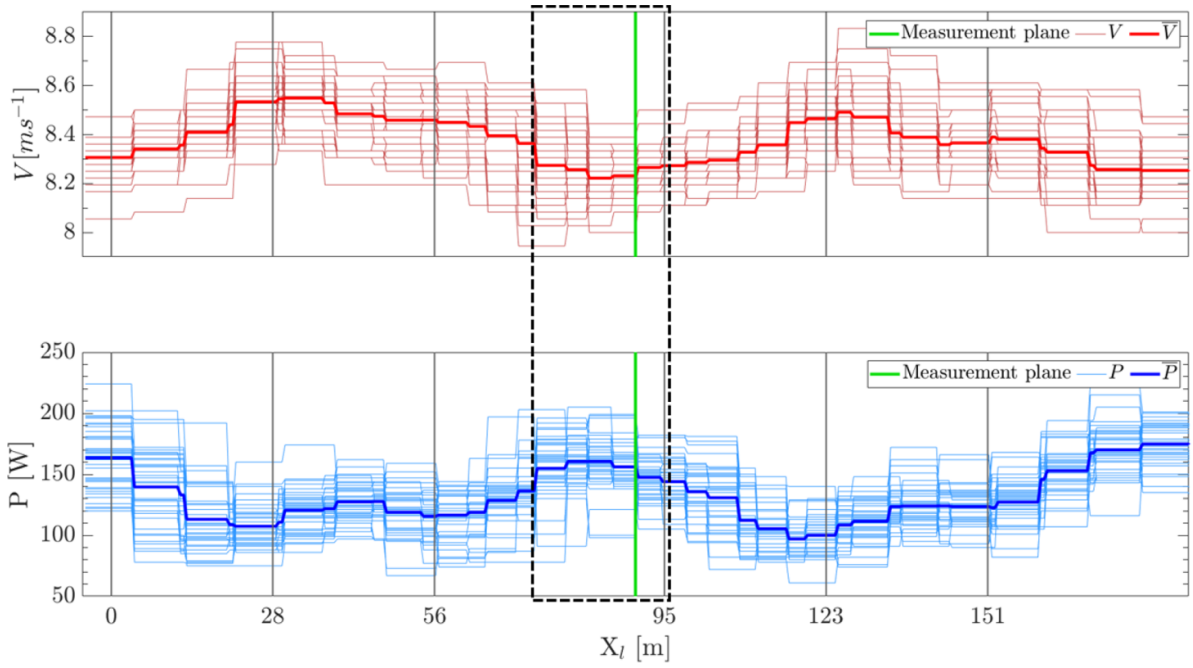

Figure 5. Instantaneous (thin lines) and phase-averaged (thick lines) velocity (top) and power (bottom) traces over the circuit. Data from the upright individual test. The RoF measurement plane location is indicated with a green vertical line.

to define the wake region behind the cyclist, which are presented in figure 6. The wake is preliminary identified with the flow region where the velocity is below a certain fixed percentage, arbitrarily set to 30%, of the minimum velocity (maximum deficit) in the flow field. Such region is then spatially dilated by a flat disk-shaped structuring element with a specified radius. The dilation length is chosen such that the entire wake and the shear layers are included in the region to be selected for the momentum analysis. The result is the control surface at the outlet S_2, recalling equation (4). The procedure for wake contouring is summarised in figure 6.

4.3.2. Mass conservation. The control volume analysis is based on the hypothesis that the net mass flow is zero across the side and top boundaries of the domain (Anderson 2011). Therefore, the shape and size of the inlet plane S_1 (figure 1) must be adapted to ensure that the mass flow rate across S_1 is equal to that across S_2. The wake contour at each measurement plane downstream (viz. after the passage) of the cyclist is adapted following the contouring approach discussed above. As initial contour upstream, the projected wake contour at the plane behind the cyclist is taken. The contour of the inlet plane is then narrowed or broadened one row of vectors at the time to reduce the mass flow difference from about 20% to below 0.1%. A graphical representation of this approach is presented in figure 7.

5. Results

5.1. A-priori uncertainty estimation

Several error sources can affect the PIV measurements, from noise in the image recordings, to peak locking and through-plane particles motion (Sciacchitano 2019). In this section, the uncertainty of the estimated drag is evaluated based on linear error propagation for the case where the velocity measurements are affected by random errors ε, whereas the systematic errors are negligible. The linear error propagation is performed in the wind tunnel frame of reference (frame of reference moving with the model). Furthermore, two simplifying assumptions are made: (a) the upstream and downstream planes are sufficiently far from the object, so that the static pressure in both planes is undisturbed and equal to p_∞; (b) there is a uniform inflow. Based on these assumptions, the aerodynamic drag of the cyclist simplifies to:

$$D = \rho \iint_A (u_\infty - u) \cdot u dS \tag{8}$$

Where u_∞ is the freestream velocity seen by the cyclist, and u is the streamwise velocity component behind the cyclist, in a cross-section of area A. Assuming that the latter velocity component is affected by a (spatially varying) random error ε:

$$u = u_{true} + \varepsilon \tag{9}$$

being u_{true} the actual velocity in the wake of the cyclist, the expression of the drag becomes:

$$\begin{aligned} D &= \rho \iint_A (u_\infty - u_{true} - \varepsilon) \cdot (u_{true} + \varepsilon)\, dA = \\ &= \rho \iint_A (u_\infty - u_{true}) \cdot u_{true} dA - \rho \iint_A \varepsilon\, (u_{true} + \varepsilon)\, dA = \\ &= D_{true} - \rho \iint_A \varepsilon\, (u_{true} + \varepsilon)\, dA \end{aligned} \tag{10}$$

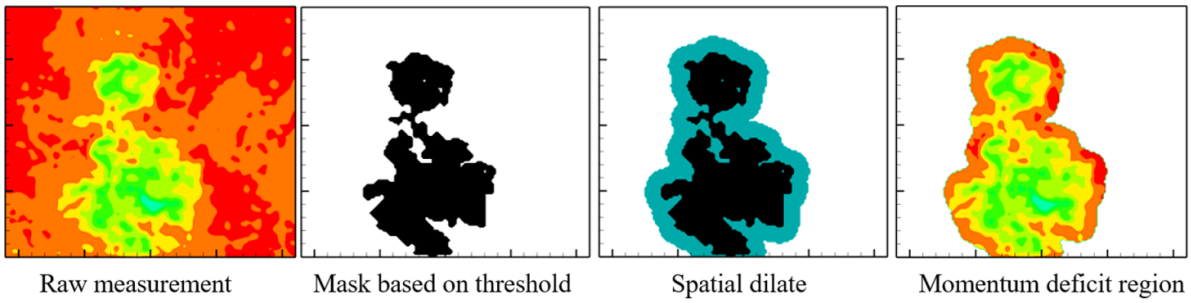

Figure 6. Flow schematic of wake contouring procedure. Explanatory movie available online.

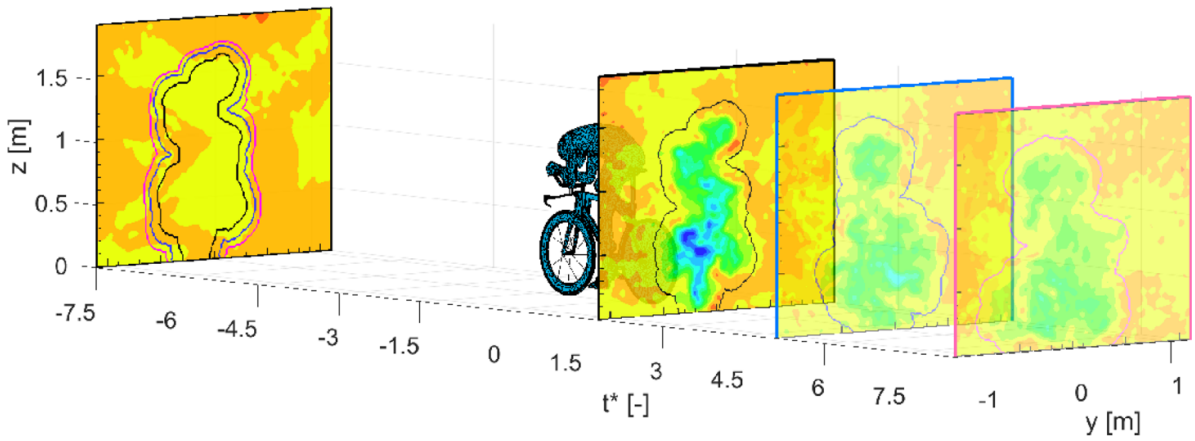

Figure 7. Contour adaptation based on the identification of the wake region (downstream plane) and compliance with the conservation of mass (upstream plane; contour colour corresponds to colour framing of the wake plane).

Where D_{true} is the true aerodynamic drag, in absence of measurement errors on the velocity. The expression of the time-averaged drag thus becomes:

$$\bar{D} = \bar{D}_{true} - \rho \iint_A \sigma_\varepsilon^2 dA \tag{11}$$

Being $\sigma_\varepsilon^2 = \overline{\varepsilon^2}$the variance of the velocity error, and having assumed that error and velocity are uncorrelated: $\overline{\varepsilon \cdot u_{true}} = 0$. From equation (11), it follows that a random error in the velocity field leads to an underestimation of the drag. The latter scales with the variance of the random error and with the area of integration. This result clarifies the importance of reducing the region of momentum analysis to the minimum, i.e. only encompassing the region of deficit. It is, however, of great importance that the domain captures the full wake for the entire duration of the measurement, otherwise an even larger underestimation of the drag may occur. For this reason, it is concluded that for the use of the Ring of Fire in an *in-vivo* environment, the best results in terms of accuracy of the drag evaluation are obtained after applying a dedicated wake contour as described in section 4.3.

In order to confirm the results from the *a-priori* uncertainty estimation, a Monte Carlo simulation is conducted on the flow field around a sphere with diameter $d = 10$ cm, obtained from a steady-state solver for incompressible, turbulent flow, using the SIMPLE algorithm with the standard k-Omega SST turbulence model (Wilcox 2008). The simulation is performed in a volume of 20 × 20 × 25 sphere diameters (W × H × L). The inlet velocity is set to 2 m s^{-1}, resulting in a Reynolds number of 1.4 × 10^4. Errors with Gaussian distribution are imposed to the streamwise velocity component in the wake plane 7.5 diameters downstream of the sphere. The relative standard deviation of the random error in the streamwise velocity $(\sigma_\varepsilon/u_\infty)$ is varied in the range from 0 to 3.5%. Consistently with equation (11), figure 8 confirms that the measured drag is underestimated in presence of measurement errors in the velocity, and that the measured drag decreases quadratically with increasing measurement errors in the velocity. Furthermore, the effect of the size of the cross-sectional area is investigated by cropping the original measurement region from all sides. Terra *et al* (2018) already identified the issue of errors arising from the size of the domain used for the momentum analysis; the authors showed that a reduction in cross-sectional area of the measurement domain could potentially lead to a reduction in the uncertainty of the measured drag by 10%. From the current analysis it is observed that, as expected, the systematic errors scale with the extent of the measurement domain considered for the drag estimation. If however, the domain is cropped so that part of the wake velocity deficit is cut off (area 4 in figure 8), consequently, the drag value is underestimated. In

the current case of the sphere, this led to an underestimation of 30% even in absence of any measurement errors in the velocity.

Assuming a typical uncertainty of the in-plane velocity components $(\sigma_{u_y}, \sigma_{u_z})$ measured by the Ring of Fire system equal to 0.1 pixel (Westerweel 1993), the uncertainty of the out-of-plane velocity component can be estimated using equation (12) (Prasad 2000), and is equal to 1% and 0.4% of the cyclist's velocity for $\theta = 20$ and 45 degrees, respectively.

$$\sigma_\varepsilon = \frac{\sigma_{u_{y,z}}}{\sqrt{2}\tan\theta} \tag{12}$$

Considering a ratio of measurement area over cyclist frontal area of 47, then, based on the Monte Carlo simulation results, the measured drag is underestimated by 3.5% and 1% for stereoscopic angles of 20 and 45 degrees, respectively.

5.2. Effect of mass conservation

In previous Ring of Fire experiments (Terra *et al* 2017, 2018, Spoelstra *et al* 2019), mass conservation in the measurement plane between before and after the passage was only assumed but never imposed. However, such assumption is not generally valid. In the current experiment, due to the rider's motion, an out-of-plane velocity of 2 m s^{-1} and a 0.4 m s^{-1} in-plane motion of the surrounding air were induced in the measurement plane. This led to a difference in the mass flow rate before and after passage of the cyclist of the order of 20%. The sensitivity of the drag estimate to the mass conservation is presented hereafter for the cyclist in time trial position with aerodynamic helmet. In literature, the drag area of a cyclist in time trial position is reported to be between 0.2–0.3 m^2 (Crouch *et al* 2017); the value measured via power meter measurements falls in that range, being 0.247 ± 0.008 m^2. Without imposing mass conservation, the drag obtained by the Ring of Fire is largely overestimated (0.447 ± 0.015 m^2). Instead, when conservation of mass is imposed by applying the approach discussed in section 4.3, the estimated drag area becomes equal to 0.211 ± 0.008 m^2, showing much better agreement with the power meter measurement. This same trend is observed for the other two test cases, namely cyclist in time trial position with road helmet the cyclist in upright position: without mass conservation the value of the drag area is overestimated by approximately 100%, whereas when mass conservation is imposed, the estimated drag area agrees with the power meter measurements within 20%.

5.3. Sensitivity to the measurement's spatial resolution

The spatial resolution of the PIV technique is an important parameter characterizing the overall measurement performance. The PIV cross-correlation analysis with a finite interrogation window (IW) size is known to return a spatially filtered velocity field (Raffel *et al* 2018); the amount of spatial filtering is expected to affect the accuracy of the drag estimate via the control volume approach. Although the simplest way to enhance the spatial resolution is to reduce the interrogation window size, this is accomplished at the cost of increasing uncertainty (Sciacchitano *et al* 2013). Hence, given the camera resolution, a compromise needs to be found between an image size large enough to capture the full wake and an interrogation window small enough to capture the small scale structures, while still providing an appropriate signal to noise ratio to minimise the number of spurious velocity vectors as well as the uncertainty on the estimated drag. The effects of the IW size on the velocity fields and on the estimated drag are investigated for 30 runs of the baseline case (time trial posture + aerodynamic helmet). The size of the IW is varied from 8×8 pixels^2 (8×8 mm^2) to 512×512 pixels^2 (512×512 mm^2). The interrogation windows are weighted with a Gaussian function, and the overlap factor between adjacent windows is kept constant at 75% for all cases. The details of the spatial resolution analysis are summarized in table 1.

The velocity fields reported in figure 9 show that the use of a large interrogation window (512×512 mm^2) yields an underestimation of the peak entrainment velocity in the cyclist's wake. The latter is caused by spatial modulation whereby the cross-correlation estimation of the convex velocity distribution produces a less-than-average value; conversely, the use of a small interrogation window (16×16 mm^2) is not visibly affected by spatial modulation, but random errors occasionally appear due to the spurious occurrence of region with a low seeding concentration. The spatial modulation in the velocity field has clear consequences on the drag area: over the first 5 m of the wake, the multi-passage average drag area (red curve in figure 9-right) for the 512×512 mm^2 IW is lower than that computed with the 64×64 and 16×16 mm^2 windows, especially in the near wake where the peak velocities are higher. The uncertainty of the measured drag area is approximately constant (~0.016 m^2, or 7% of the measured value) for interrogation window sizes between 16×16 mm^2 and 128×128 mm^2, which indicates the low sensitivity to the PIV spatial resolution in this range of interrogation window sizes. In contrast, higher uncertainty is retrieved for smaller interrogation windows (8×8 mm^2, uncertainty of 0.018 m^2 or ~10% of the measured value) due to the dramatic loss of the cross-correlation signal-to-noise ratio which causes large measurement errors in the velocity fields, as well as for larger interrogation windows (exceeding 256×256 mm^2) due to spatial modulation effects that cause a larger spread in drag area between the different runs. Hence, the size of IW should be within 0.05 c and 0.25 c, where c is the characteristic length scale representative for the wake topology (shoulder width in this case). Choosing a larger IW leads to errors due to modulation; smaller IW size, on the other hand, leads to an increase in uncertainty due to random errors. This is, however, very dependent on experimental settings such as seeding density and pixel size of the camera. Based on the considerations above, the final interrogation window size value of 64×64 mm^2 has been selected for the results presented in the remainder of this work as a compromise between high spatial resolution and low measurement errors in the velocity fields.

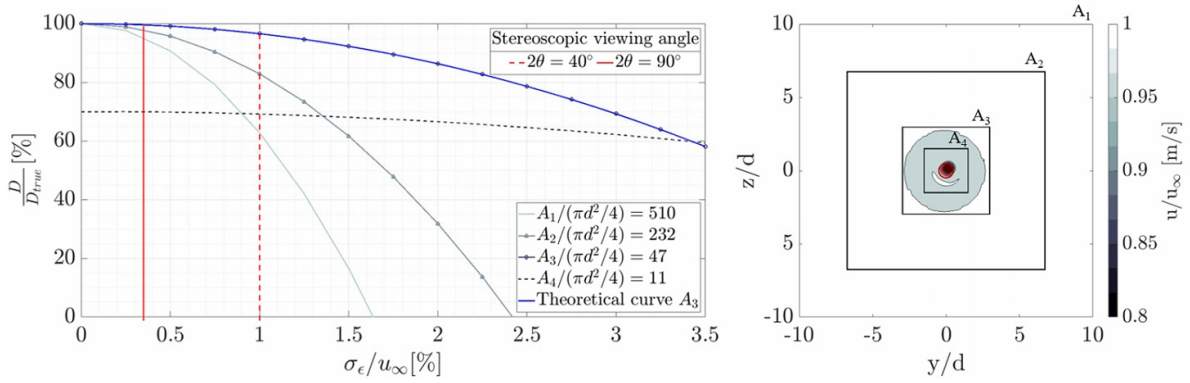

Figure 8. Uncertainty on drag area propagated from random error in the out-of-plane velocity for different wake plane sizes.

Table 1. Effect of the interrogation window size on the cross-correlation signal-to-noise ratio (SNR) and the estimated drag area (C_dA).

IW size [mm^2]	Image density [particles/IW]	Vector pitch [mm]	Correlation$\overline{SNR}$	$\overline{\overline{C_dA}}$ [m^2]	±95% CI [m^2]
8 × 8	0.5–1	2	1.6	0.191	±0.027
16 × 16	2–5	4	1.9	0.204	±0.018
32 × 32	8–20	8	2.1	0.203	±0.016
64 × 64	30–70	16	3.0	0.204	±0.007
128 × 128	100–300	32	4	0.202	±0.007
256 × 256	500–1200	64	6	0.198	±0.008
512 × 512	2000–5000	128	8	0.183	±0.016

5.4. Comparison to drag estimation from power meter data

The multi-passage average drag $\left(\overline{C_dA_{multi}}\right)$ of the three different test cases obtained from the Ring of Fire is compared to the average drag estimated from the power meter data. The measurements were acquired simultaneously, so the average results are obtained from the same set of samples for both the Ring of Fire and the power meter.

Firstly, the drag areas obtained from the RoF are considered. As was presented in section 2.2, in order to obtain the multi-passage average drag $\left(\overline{C_dA_{multi}}\right)$ per test case, first the drag area in the wake of the single passages needed to be time-averaged to reduce the effect of the unsteady fluctuations. The wake is divided into two regions, namely the near and the far wake. In the near wake region, within five characteristic length scales from the cyclist, pressure effects cannot be disregarded according to Terra *et al* (2017). Considering as characteristic length the shoulder width of the cyclist $c = 0.5$ m, it follows that the static pressure in the flow affects the cyclist's drag estimate for the first 2.5 m downstream of the rider. Furthermore, the rider transited the laser sheet with no predefined crank-angle, meaning that the crank-angle at the laser sheet location varied from run to run. Spoelstra *et al* (2019) report the information of the pedal position is maintained in the near wake, but not in the far wake due to turbulent mixing of the flow. For the upright case, this led to a computed drag area of 0.257 m^2, with a 95% confidence level uncertainty of 0.012 m^2. For the time-trial position, the drag are reduces to 0.211 m^2 when the rider wears a time trial helmet, and to 0.226 m^2 when the road helmet is used. The uncertainties of these values are 0.008 m^2 and 0.010 m^2, respectively, at 95% confidence level.

The average drag areas per test cases computed from the power meter data follow the methodology and processing steps explained in sections 2.1 and 4.1. The final values are presented in figure 10 together with the above mentioned values from the RoF.

The results in figure 10 can be analysed in two different ways, namely by assessing the relative difference of the measurement techniques between each test condition, or by evaluating the absolute values of the predicted drag area. Regarding the absolute values, it is observed that the power meter approach on average overestimates the drag by 20% compared to the RoF. Additionally, the drag values obtained with the two techniques do not agree within the respective uncertainty bands. These disagreements can be ascribed to systematic errors in both the RoF approach, as described in section 5.1, and in the power meter measurements due to the simplified power meter model (e.g. flat road) and of the uncertainty in the model constants (e.g. rolling resistance coefficient), as discussed in section 2.1. While the latter error sources affect the absolute drag estimates obtained with the power meter, they cancel out when considering relative drag variations. Therefore, considering the relative performance, the trends of the power meter and the Ring of Fire measurements show good agreement, as a large-scale drag increase from time-trial to upright position is obtained. While the Ring of Fire predicts an increase in drag area of 0.049 m^2 (23%), the power meter results increase by 0.066 m^2 (27%). Between the two helmet types, a small-scale increase of 0.015 m^2 (7%) can

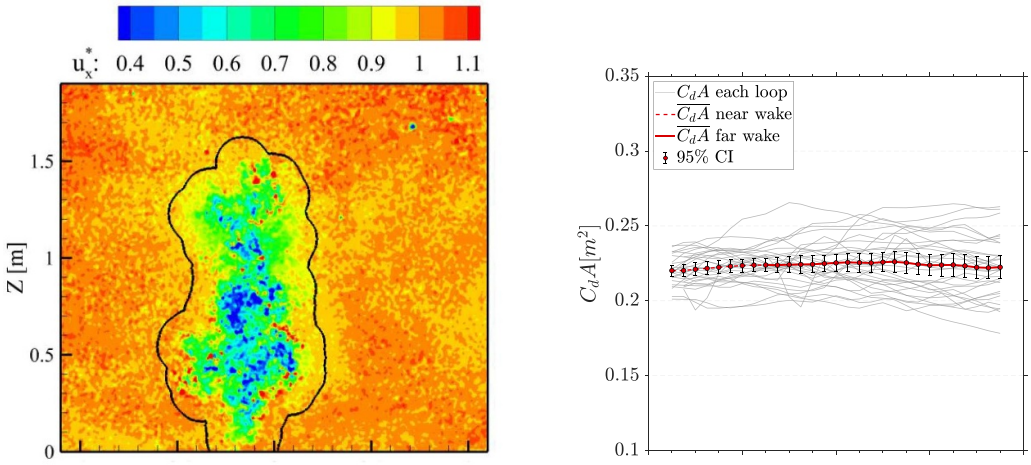

(a) Window size: 16 × 16 [mm ^{2}]

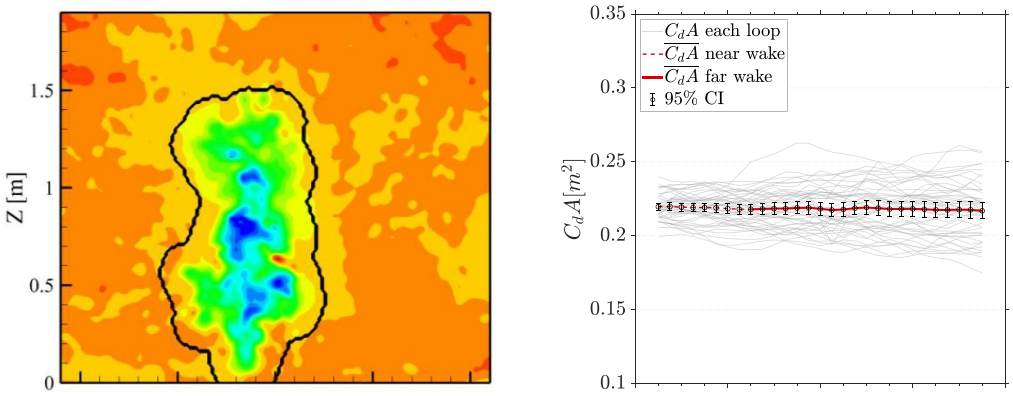

(b) Window size: 64 × 64 [mm^2]

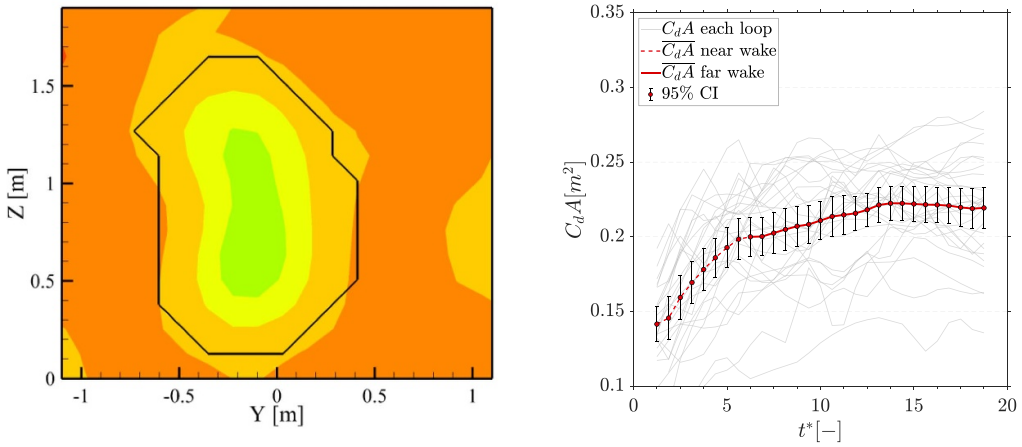

(c) Window size: 512 × 512 [mm^2]

Figure 9. Dimensionless instantaneous streamwise velocity (u_x^*) at $t^* = 1$ (left) and streamwise C_dA evolution in the wake (right). Data from the individual test in time trial position with aerodynamic helmet. The black lines represent the wake contours used for the drag analysis. (a) Window size: 16 × 16 [mm^2]. (b) Window size: 64 × 64 [mm^2]. (c) Window size: 512 × 512 [mm^2].

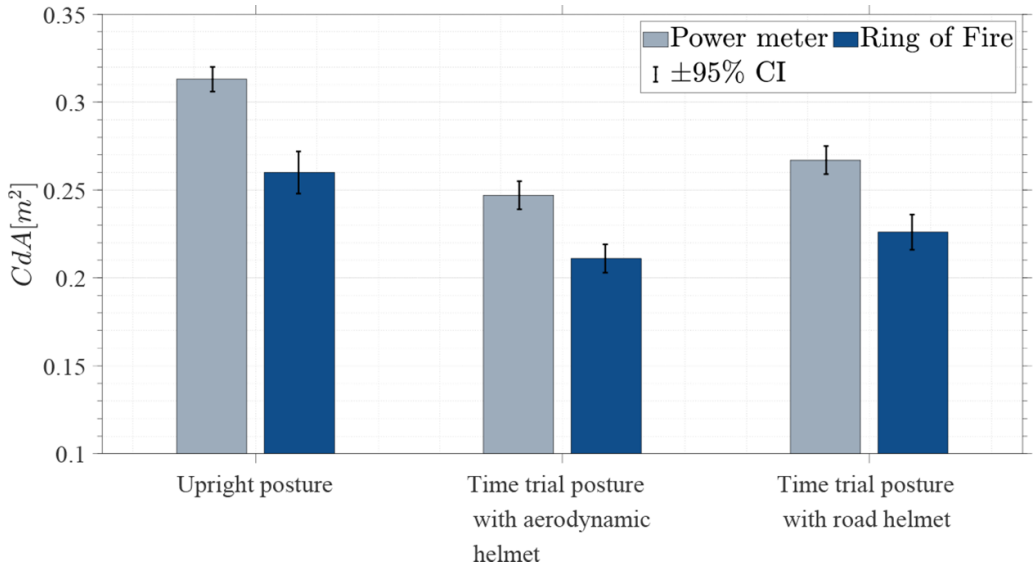

Figure 10. Comparison between the average drag area from the RoF and Power meter for the different configurations; uncertainty bars for 95% confidence interval.

be extracted from the Ring of Fire measurements, compared to a delta of 0.020 m^2 (8%) for the power meter approach.

6. Conclusions

In this work, large-scale stereo-PIV measurements are conducted to determine the aerodynamic drag of a moving cyclist using the control volume approach. The flow is measured in the wake of a cyclist moving at 8.3 m s^{-1}. The single-passage and multi-passage average aerodynamic drag is evaluated via a control volume approach along the wake behind the cyclist, accounting for the non-uniform flow conditions prior to the cyclist's passage. A sensitivity analysis takes into account key parameters of the PIV technique, namely the interrogation window size and the control volume formulation, specifically determining the boundaries of the control volume. It is found that applying a dedicated wake contour and imposing the conservation of mass results in the most accurate drag measurements. Furthermore, the IW size should be within 0.05 c and 0.25 c, where c is the characteristic length scale representative for the wake topology. Finally, the drag values obtained with the RoF are compared against the drag estimates from simultaneously acquired power meter data. To assess the agreement between the two approaches in different regimes, three individual tests are performed where small drag variations due to different helmets as well as large drag variations due to different cyclist postures are produced. Regardless of the underlying input parameters in the power meter model, both small- and large scale deltas are well captured by both the Ring of Fire technique and the power meter approach and agree with available literature values (Blair *et al* 2009, Barry *et al* 2014, Spoelstra *et al* 2019). The uncertainty on the average drag measurements from the RoF is within 5%. Although such value is considered rather coarse when compared with state-of-the-art force balance measurements conducted in a wind tunnel, it shows great potential for a range of other applications (drones, cars, trains, birds, …) due to the possibility to determine the aerodynamic drag in-field rather than in the lab environment and simultaneously obtain flow visualization.

Acknowledgments

This research is supported by the Netherlands Organisation for Scientific Research (NWO) Domain Applied and Engineering Sciences (TTW), project 15583 'Enabling on-site sport aerodynamics with the Ring of Fire'. The Team Sunweb provided part of the cycling equipment for both experiments. We thank Albert Timmer and Floortje Mackaij riding a combined 550 laps or 105 km during the experiments. Edoaro Saredi is kindly acknowledged for supporting the CFD simulations.

Data and supplementary movies

The data presented in this publication is available at: doi:10.4121/uuid:c8a6c2a7-7278-43eb-b8aa-7a0fb4b2160d. Supplementary movies are (available online at stacks.iop.org/MST/32/044004/mmedia)

ORCID iDs

A Spoelstra https://orcid.org/0000-0002-1876-1612
A Sciacchitano https://orcid.org/0000-0003-4627-3787
F Scarano https://orcid.org/0000-0003-2755-6669

References

Adrian L, Adrian R J and Westerweel J 2011 *Particle Image Velocimetry* (Cambridge: Cambridge University Press)
Adrian 1997 Dynamic ranges of velocity and spatial resolution of particle image velocimetry *Meas. Sci. Technol.* **8** 1393–8

Anderson J D 2011 *Fundamentals of Aerodynamics* (New York: McGraw-Hill)

Baldissera P and Delprete C 2016 Rolling resistance, vertical load and optimal number of wheels in human-powered vehicle design *Proc. Inst. Mech. Eng.* P **231** 33–42

Barlow J B, Rae W H, Pope A and Pope A 1999 *Low-speed Wind Tunnel Testing* (New York: Wiley)

Barry N, Burton D, Sheridan J, Thompson M and Brown N 2014 Aerodynamic performance and riding posture in road cycling and triathlon *Proc. Inst. Mech. Eng.* p **229** 28–38

Bell J R, Burton D, Thompson M C, Herbst A H and Sheridan J 2015 Moving model analysis of the slipstream and wake of a high-speed train *J. Wind Eng. Ind. Aerodyn.* **136** 127–37

Bertucci W, Duc S, Villerius V, Pernin J N and Grappe F 2005 Validity and reliability of the powertap mobile cycling powermeter when compared with the SRM device *Int J Sports Med* **26** 868–73

Bierman J 2016 *Tire Test - Vittoria Corsa G+ (Tubular)* (available at: www.bicyclerollingresistance.com)

Blair K and Sidelko S 2009 Aerodynamic performance of cycling time trial helmets (P76) *The Engineering of Sport 7* (Berlin: Springer) pp 371–8

Bosbach J, Kühn M and Wagner C J E I F 2009 Large scale particle image velocimetry with helium filled soap bubbles *Exp. Fluids* **46** 539–47

Burke E R 2003 *High Tech Cycling the Science of Riding Faster* (Champaign, IL: Human Kinetics)

Coutanceau M and Bouard R 1977 Experimental determination of the main features of the viscous flow in the wake of a circular cylinder in uniform translation. Part 2. Unsteady flow *J. Fluid Mech.* **79** 257–72

Crouch T N, Burton D, Brown N A T, Thompson M C and Sheridan J 2014 Flow topology in the wake of a cyclist and its effect on aerodynamic drag *J. Fluid Mech.* **748** 5–35

Crouch T N, Burton D, Labry Z A and Blair K B 2017 Riding against the wind: a review of competition cycling aerodynamics *Sports Eng.* **20** 81–110

Debraux P, Grappe F, Manolova A V and Bertucci W 2011 Aerodynamic drag in cycling: methods of assessment *Sports Biomech.* **10** 197–218

Duc S, Villerius V, William B and Grappe F 2007 Validity and reproducibility of the ergomo® pro power meter compared with the SRM and powertap power meters *Int. J. Sports Physiol. Perform* **2** 270–81

Edwards A G and Byrnes W C 2007 Aerodynamic characteristics as determinants of the drafting effect in cycling *Med. Sci. Sports Exerc* **39** 170–6

Faleiros D E, Tuinstra M, Sciacchitano A and Scarano F 2019 Generation and control of helium-filled soap bubbles for PIV *Exp. Fluids* **60** 40

Grappe F, Candau R, Belli A and Rouillon J D 1997 Aerodynamic drag in field cycling with special reference to the Obree's position *Ergonomics* **40** 1299–311

Griffith M, Crouch T, Thompson M, Burton D, Sheridan J and Brown N 2014 Computational fluid dynamics study of the effect of leg position on cyclist aerodynamic drag *J. Fluids Eng.* **136** 101105

Hedenström A and Johansson L C 2015 Bat flight: aerodynamics, kinematics and flight morphology *J. Exp. Biol.* **218** 653–63

Henning A, Richard H, Kowalski T, Gries T, Huntgeburth S and Loose S 2016 *Full scaled high speed train PIV measurement*

Jones B 1936 *Measurement of Profile Drag by the Pitot-traverse Method* 1688 (London: H.M. Stationery Office)

Khayrullina A, Blocken B, Janssen W and Straathof J 2015 CFD simulation of train aerodynamics: train-induced wind conditions at an underground railroad passenger platform *J. Wind Eng. Ind. Aerodyn.* **139** 100–10

Kurtulus D F, Scarano F and David L 2007 Unsteady aerodynamic forces estimation on a square cylinder by TR-PIV *Exp. Fluids* **42** 185–96

Kyle C R 2001 The mechanical efficiency of bicycle derailleur and hub gear transmissions *Human Power* **52** 3

Laitone E V 1997 Wind tunnel tests of wings at Reynolds numbers below 70 000 *Exp. Fluids* **23** 405–9

Le Good G M, Howell J P, Passmore M A and Cogotti A 1998 A comparison of on-road aerodynamic drag measurements with wind tunnel data from pininfarina and MIRA *SAE Trans.* **107** 967–76

Lukes R, Hart J and Haake S 2012 An analytical model for track cycling *Proc. Inst. Mech. Eng. P* **226** 143–51

Martin J, Milliken D, Cobb J, Mcfadden K and Coggan A 1998 Validation of a mathematical model for road cycling power *J. Appl. Biomech.* **14** 276–91

Matschke G and Heine C 2002 *Full Scale Tests on Side Wind Effects on Trains. Evaluation of Aerodynamic Coefficients and Efficiency of Wind Breaking Devices* (Berlin, Heidelberg: Springer) (https://doi.org/10.1007/978-3-540-45854-8_3)

Olds T 2001 Modelling Human Locomotion *Sports Med.* **31** 497–509

Páscoa J, Brojo F, Charrua Santos F and Fael P 2012 An innovative experimental on-road testing method and its demonstration on a prototype vehicle *J. Mech. Sci. Technol.* **26** 1663–70

Passfield L, Hopker J G, Jobson S, Friel D and Zabala M 2017 Knowledge is power: issues of measuring training and performance in cycling *J. Sports Sci.* **35** 1426–34

Passmore M A and Jenkins E G 1988 *A Comparison of the Coastdown and Steady State Torque Methods of Estimating Vehicle Drag Forces* (https://doi.org/10.4271/880475)

Prasad A K 2000 Stereoscopic particle image velocimetry *Exp. Fluids* **29** 103–16

Raffel M, Willert C E, Scarano F, Kähler C J, Wereley S T and Kompenhans J 2018 *Particle Image Velocimetry: A Practical Guide* (Berlin: Springer)

Rival D E and Oudheusden B 2017 Load-estimation techniques for unsteady incompressible flows *Exp. Fluids* **58** 20

Samimy M and Lele S K 1991 Motion of particles with inertia in a compressible free shear layer *Phys. Fluids* **3** 1915–23

Scarano F 2001 Iterative image deformation methods in PIV *Meas. Sci. Technol.* **13** R1–R19

Scarano F, Ghaemi S, Caridi G, Bosbach J, Dierksheide U and Sciacchitano A 2015 On the use of helium-filled soap bubbles for large-scale tomographic PIV in wind tunnel experiments *Exp. Fluids* **56** 42

Scarano F, van Wijk C and Veldhuis L J E I F 2002 Traversing field of view and AR-PIV for mid-field wake vortex investigation in a towing tank *Exp. Fluids* **33** 950–61

Sciacchitano A 2019 Uncertainty quantification in particle image velocimetry *Meas. Sci. Technol.* **30** 092001

Sciacchitano A, Wieneke B and Scarano F 2013 PIV uncertainty quantification by image matching *Meas. Sci. Technol.* **24** 045302

Spedding G R and Hedenström A 2010 PIV-based investigations of animal flight *Animal Locomotion*, ed G K Taylor, M S Triantafyllou and C Tropea (Berlin, Heidelberg: Springer Berlin Heidelberg) pp 187–201

Spicer J, Richardson C, Ehrlich M, Bernstein J, Fukuda M and Terada M 2001 Effects of frictional loss on bicycle chain drive efficiency *J. Mech. Design* **123** 598–605

Spoelstra A, de Martino Norante L, Terra W, Sciacchitano A and Scarano F 2019 On-site cycling drag analysis with the Ring of Fire *Exp. Fluids* **60** 90

Terra W, Sciacchitano A and Scarano F 2017 Aerodynamic drag of a transiting sphere by large-scale tomographic-PIV *Exp. Fluids* **58** 83

Terra W, Sciacchitano A, Scarano F and van Oudheusden B W 2018 Drag resolution of a PIV wake rake for transiting models *Exp. Fluids* **59** 120

Terra W, Sciacchitano A and Shah Y H 2019 Aerodynamic drag determination of a full-scale cyclist mannequin from large-scale PTV measurements *Exp. Fluids* **60** 29

Tschepe J, Nayeri C N and Paschereit C O 2019 Analysis of moving model experiments in a towing tank for aerodynamic drag measurement of high-speed trains *Exp. Fluids* **60** 98

Underwood L 2012 *Aerodynamics of Track Cycling* Doctoral, University of Canterbury, Canterbury

Usherwood J R, Cheney J A, Song J, Windsor S P, Stevenson J P J, Dierksheide U and Bomphrey R J 2020 High aerodynamic lift from the tail reduces drag in gliding raptors *J. Exp. Biol.* **223** jeb214809

von Carmer C F, Heider A, Schröder A, Konrath R, Agocs J, Gilliot A and Monnier J-C 2008 Evaluation of large-scale wing vortex wakesfrom multi-camera PIV measur-ements in free-flight laboratory *Particle Image Velocimetry: New Developments and Recent Applications* (Berlin, Heidelberg: Springer Berlin Heidelberg) pp 377–94

Watkins S, Saunders J W and Kumar H 1992 Aerodynamic drag reduction of goods trains *J. Wind Eng. Ind. Aerodyn.* **40** 147–78

Westerweel J 1993 Digital particle image velocimetry: Theory and application (Netherlands: Delft University)

Westerweel J and Scarano F 2005 Universal outlier detection for PIV data *Exp. Fluids* **39** 1096–100

Wilcox D C 2008 Formulation of the k-w turbulence model revisited *AIAA* **46** 2823–38

Zdravkovich M M 1990 Conceptual overview of laminar and turbulent flows past smooth and rough circular cylinders *J. Wind Eng. Ind. Aerodyn.* **33** 53–62